

Ultra-miniaturized dual-band implantable antenna for retinal prosthesis

Abdelmouttalib Bousrout¹, Asma Khabba², Saida Ibnyaich², Tomader Mazri¹, Mohamed Habibi³,
Tole Sutikno⁴

¹Laboratory of Advanced Systems Engineering, National School of Applied Sciences, Ibn Tofail University, Kenitra, Morocco

²Instrumentation, Signals and Physical Systems (I2SP) Team, Faculty of Sciences SEMLALIA, Cadi Ayyad University, Marrakesh, Morocco

³Laboratory of Electronic Systems, Information Processing, Mechanics and Energetics, Faculty of Science, Ibn Tofail University, Kenitra, Morocco

⁴Master Program of Electrical Engineering, Faculty of Industrial Technology, Universitas Ahmad Dahlan, Yogyakarta, Indonesia

Article Info

Article history:

Received Mar 17, 2024

Revised Aug 5, 2024

Accepted Aug 26, 2024

Keywords:

Dual-band

Implantable antenna

Retinal prosthesis

Specific absorption rate

ABSTRACT

This article presents two miniaturized antennas designed for retinal prosthesis devices, aimed at enhancing vision for blind individuals with functional optic nerves. The implantable antenna is 2.2 mm wide, 2.15 mm tall, and 0.78 mm thick. It works in the ISM bands but is small because it uses slot incorporation and high-permittivity substrates. High-frequency structure simulator (HFSS) electromagnetic simulations show great performance, with a 16.66% impedance bandwidth at 2.4 GHz and a 10.34% bandwidth at 5.8 GHz. The peak gain values are -27.76 dB at 2.4 GHz and -16.40 dB at 5.8 GHz. We have also developed an extraocular antenna for telemetry and energy transfer, with dimensions of 36×36×1.6 mm³. Validation through CST calculation software confirms the efficacy of both antenna designs. Implantable antennas hold significant promise in biomedical antenna research, demonstrating capabilities conducive to retinal implantation and offering potential advancements in vision restoration technology.

This is an open access article under the [CC BY-SA](https://creativecommons.org/licenses/by-sa/4.0/) license.



Corresponding Author:

Asma Khabba

Instrumentation, Signals and Physical Systems (I2SP) Team, Faculty of Sciences SEMLALIA

Cadi Ayyad University

Marrakesh, Morocco

Email: khabba.asma@gmail.com

1. INTRODUCTION

Integrated medical devices (IMDs) have enhanced people's quality of life, regardless of their health status. IMDs have the ability to monitor patients' vital signals and notify doctors of their critical conditions [1]. To ensure patient comfort and maximize benefits, these devices need to communicate wirelessly with outdoor equipment. To overcome the limitations of inductive biotelemetry, such as low information rate, limited range, and sensitivity, many researchers have expressed great interest in biotelemetry antennas. In order to tackle the problems of miniaturization, as well as other challenges and restrictions, such as biocompatibility, impedance matching, link budget, and patient safety, implantable antennas are of significant scientific interest [2]. IMDs use a variety of frequency bands, including the medical implant communication service (MICS) band (402-405 MHz), which is an unlicensed service for biomedical applications recognized worldwide. However, the ISM bands vary from country to country. In the US, the federal communications commission (FCC) regulates and structures the ISM bands (902–928 MHz and

2400–2483.5 MHz). Typically, devices use the ISM band (2400–2483.5 MHz) to transition from standby to wake-up mode, thereby conserving battery power and prolonging the device's lifespan [3]–[5]. Wireless implanted devices widely use the MedRadio frequency band, extending from 401 to 406 MHz; however, sources [6]–[8] have indicated that antennas operating in this frequency range have limited bandwidths, leading to low data rates and limited image resolution.

Recent developments and significant challenges in the field of medically implanted antennas are discussed in [2], highlighting factors influencing radio wave propagation within the human body. Recently, there have been advancements in implanted antenna technologies for telemetry applications. For instance, in [9], a compact antenna configuration facilitated intracranial pressure monitoring (ICP) through dual communication channels at 915 MHz and 2.45 GHz, demonstrating excellent broadband performance. Another development, described in [10], involves a multi-band compatible antenna integrated into a capsule system capable of operating across MedRadio, the medium band (1200 MHz), and three ISM bands simultaneously. Despite a slight 1.5% bandwidth reduction at 402 MHz in a homogeneous muscle phantom, this antenna shows an overall bandwidth increase of 27.36%. Liapatis and Nikita [11] also talk about a small three-band antenna ($3 \times 3 \text{ mm}^2$) that is made for retinal prostheses and can achieve -4.9 dBi power on a homogeneous eye phantom and a wide 6 GHz bandwidth. According to Faisal and Yoo [12], a small dual-band antenna measuring $7.2 \times 7 \times 0.2 \text{ mm}^3$ that is meant for implantable batteries gets the best results when tested on a single-layer skin phantom, with -25.65 dBi at 928 MHz and -28.44 dBi at 2.45 GHz. Researchers found the SAR values for this antenna to exceed permissible limits [13], [14]. Additionally, Saha *et al.* [15] present a compact circularly polarized antenna specifically designed for bio-telemetry applications, measuring $10 \times 10 \times 0.3 \text{ mm}^3$. The simulated gain across the entire operating band is approximately 7.79 dBi, with accompanying SAR analysis conducted as part of the study. However, since integrated wireless medical devices (IWMDs) require operational frequencies for wireless charging and wake-up in addition to biotelemetry, single-band antennas would not be sufficient to meet all of their needs [16]. There haven't been many dual- and triple-band operating ingestible implanted antennas proposed in the literature [17]. Bahrami *et al.* [18] report the development of two pairs of small antennas for a retinal prosthesis. The intraocular antenna has a shorting pin and is triangular, measuring 7.63 mm^3 in size at 2.45 GHz. An extraocular antenna, which is also triangular, has parasitic parts and is a rectangular patch, measuring 26.24 mm^3 in size at the same frequency. At 1.45 GHz, another intraocular antenna with a size of $6.25 \times 6 \times 0.63 \text{ mm}^3$ and a second planar inverted-F extraocular antenna ($28 \times 24 \times 1.43 \text{ mm}^3$) were proposed.

We evaluated the antenna efficiency by simulating the antenna reflection and transmission coefficients, electric field strength, and SAR, and then analyzed the manufacturing process to understand the performance. However, we discovered that the presentation and discussion of antenna gains had ceased. In the literature, only a few works have focused on retinal implants. The retinal prosthesis, therefore, is a very interesting application of advanced biomedical systems comprising an extraocular unit and an implanted intraocular unit. Figure 1 shows the components of a retinal implant [19]. The system consists of an external component and an implanted component. The system attaches an external camera to the patient's spectacles and connects it to a mobile visual treatment unit, which processes the picture before transmitting it to the implant's integrated part through a transmitting antenna. The antenna serves two purposes: it wirelessly transmits radio frequency (RF) telemetry data to an internal communication antenna and transmits RF energy to deeply buried implants to power them. The patient's lens holds the implantable part in place. The implanted antenna receives the RF signal, decodes it into a signal, and then transmits it directly to the intraocular retinal stimulator via a cable.

Following an extensive literature review, this study aims to address challenges within the domain of IMDs. The ability of dual-band antennas to precisely align with targeted frequency bands and overcome tissue-related obstacles makes them highly esteemed. The primary focus is on developing high-quality biomedical antennas, specifically for applications involving retinal implants. A notable challenge in these applications is the size constraint of antennas due to the eye's small dimensions. It is imperative to reconcile this constraint with the necessity of ensuring optimal antenna performance. This research successfully tackles this challenge by engineering a compact antenna that meets size requirements while delivering exceptional performance. We identified critical performance factors such as gain, radiation efficiency, impedance matching, sensitivity, and antenna size through a comprehensive review of existing studies. We meticulously designed the antenna with these factors in mind, emphasizing wide coverage, high gain, low SAR, simplicity, and compactness to optimize performance. The results are impressive, featuring a broad impedance bandwidth of 16.66% at 2.4 GHz and 10.34% at 5.8 GHz, along with peak gain values of -27.76 dB and -16.40 dB, respectively. Remarkably, the implantable antenna is compact, measuring just $2.2 \times 2.15 \times 0.78 \text{ mm}^3$. These outcomes represent a significant leap in biomedical antenna technology, particularly for retinal implants, enhancing antenna capabilities to meet specific application requirements and laying the groundwork for future healthcare innovations. This article has the following structure: The introduction reflects on the appeal of biomedical implants, specifically the radio component of these devices, the

requirements of biomedical antennas, and some challenges. The introduction also delves into several relevant works in this application area, highlighting their strengths and drawbacks, and providing the impetus for this study. The second part covers the procedures and methods used to create the proposed implanted antenna, the simulation environment, and the discussion of the results obtained after the parametric studies. The analysis of the simulated results also covers the coupling effects resulting from the integration of the antenna in the retinal prosthesis. The next section proposes a transmission antenna that provides both telemetry and energy transfer to the implanted part of the system. The same section also examines the SAR in a heterogeneous environment using a human eye model. The final section delves into the analysis of the linkage budget for the proposed antenna, subsequently presenting a comparative study, a conclusion, and references.

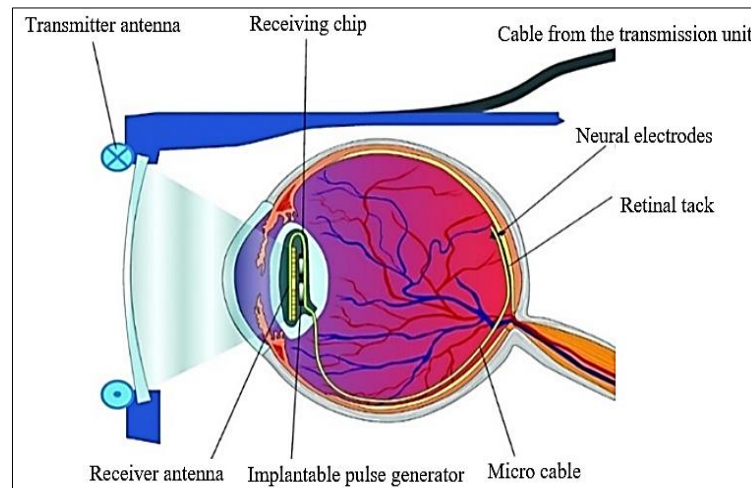


Figure 1. The architecture of the implant in the patient's eye

2. METHOD

2.1. System design and simulation environment

Figure 2 shows the architecture of the proposed retinal implant system and the simulation environment. Figure 2(a) shows that we first tested the proposed small antenna in an eyeball that has four different biological layers: the vitreous humor, the sclera, the lens, and the cornea. Each of these layers has its own dielectric properties. Table 1 shows the tissues' electrical characteristics [20]. Figure 2(b) depicts the position of the retinal implant in the phantom designed under high-frequency structure simulator (HFSS). The integrated part of the retinal implant has more than just the antenna that is implanted. It has data management, power management, a printed circuit board (PCB), a biocompatibility layer, connecting wires, an electrode array, a cable, and an electronic pack, as shown in Figure 2(b). The implant used in our study is well described in [21], [22]. The scientific literature contains several other retinal implant designs, some of which may resemble or deviate from the one we have proposed. However, our main objective is to gain a better understanding of the complex interactions between the proposed intraocular antenna and the various components of retinal implant systems. Our main concerns are twofold: firstly, proactively identifying any possible impact on the antenna's performance, especially in terms of coupling effects; and secondly, putting in place a fail-safe mechanism to make sure it works perfectly in the real world. We developed this methodology considering the worst-case scenario, where the antenna is in direct proximity to the implant itself. The first in vitro tests on the isolated retina of the tiger salamander made it possible to evaluate its effectiveness. Silicone ($\epsilon_r = 11.9$), with a thickness of 0.1 mm, encapsulates the retinal implant to prevent direct contact with tissue.

Table 1. Electrical properties of tissues used in eyeball models

Electrical properties	Frequency (GHz)	Vitreous humor	Lens	Sclera	Cornea
Relative permittivity (ϵ_r)	2.4	68.2	34	52.2	51.7
	5.8	64.8	30.5	4.78	46.5
Conductivity σ (S/m)	2.4	2.44	1.06	2	2.26
	5.8	6.67	3.43	5.47	5.66

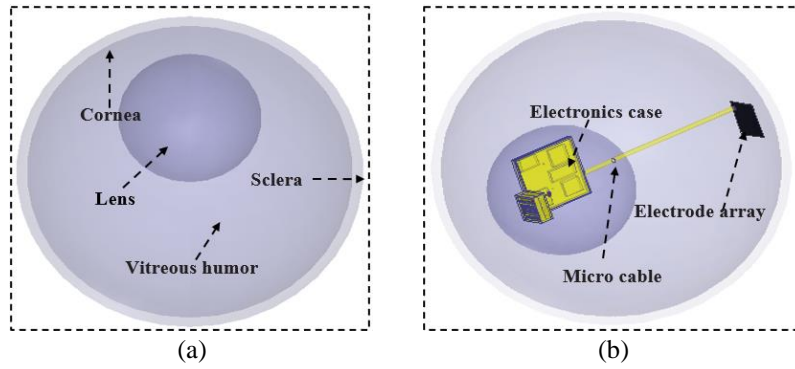


Figure 2. Architecture of proposed retinal implant system and simulation environment (a) eyeball models and (b) the position of the system in the phantom

2.2. Antenna design

Figure 3 illustrates the proposed antenna. Figures 3(a) and 3(b) show that it consists of two radiating elements stacked vertically and designed in meanders. Figure 3(c) shows the placement of these elements on a ground plane to minimize backward radiation. The antenna has a sandwich-like configuration, as illustrated in Figure 3(d). The meandering and stacking of the patches lengthen the current flow, thereby reducing the antenna's size. The dispersed tissues of the spiral and meander antennas make them less susceptible to dielectric alterations in the human body [23]. The antenna's overall size is $2.2 \times 2.15 \times 0.78 \text{ mm}^3$. Table 2 illustrates the essential dimensions of the studied antenna, highlighting its length, width, and height, as well as the characteristics of the slots in the ground plane and the patch. We etch the antenna's top patch on FR4 epoxy material and print the lower patch on Rogers TMM10, both of which have thicknesses of 0.4 mm and 0.38 mm. The TMM10 material's high permittivity aids in miniaturization by decreasing antenna losses and effective wavelength [24]. We feed the two patches with a coaxial wire with an impedance of 50 ohms, and we connect the bottom patch to the ground plane via a low-resistance chip with $R=5 \text{ ohm}$. For miniaturization and matching, we add a 3.5-ohm resistor to the upper patch. Finally, we apply a thin layer of silicon to the antenna to ensure biocompatibility.

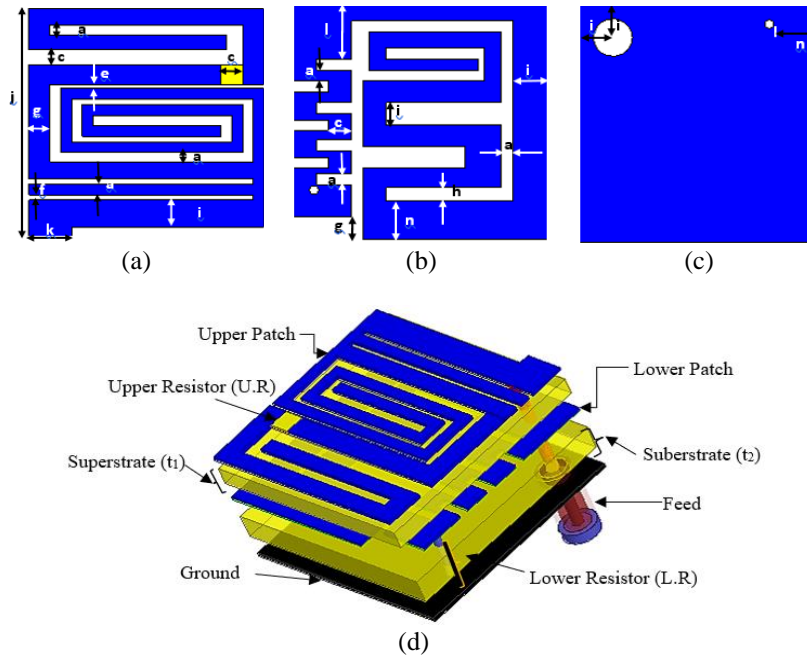


Figure 3. The structure of the implantable antenna being proposed: (a) top patch, (b) ground plane, (c) bottom patch, and (d) side view

Table 2. List of the parameters of the stated design

Parameter	a	b	c	e	f	j	h
Dimension (mm)	0.1	2.2	0.16	0.08	0.09	2.15	0.22
Parameter	g	k	l	n	t ₁	t ₂	i
Dimension (mm)	0.13	0.4	0.26	0.23	0.4	0.38	0.2

2.3. Designing steps

This section describes the ultra-miniature antenna's architecture using the 5.725-5.875 GHz and 2.4-2.48 GHz frequencies. Figure 4 displays the proposed antenna's design process. Figure 5 shows the reflection coefficient as a function of frequency for the various design steps. The final structure evolved over three design and optimization models. It is evident that minor adjustments to the rectangular (upper and lower) patches led to the final design. In addition to the spiral shape of the radiating elements, other modifications included inserting resistors on the upper and lower patches to improve performance and miniaturize the antenna. We did not make any changes to the ground plane because using a full ground plane does not result in any power flow to the rear. We conducted a thorough parametric analysis based on the reflection coefficient before choosing the patch shapes. The antenna improves with incremental changes in its design, as shown in Figure 4.

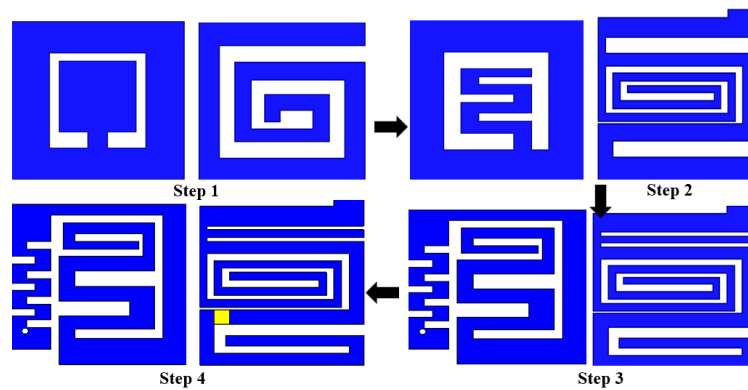


Figure 4. Designing steps

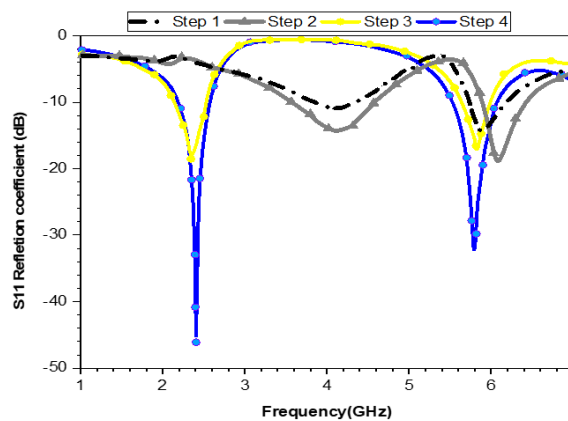


Figure 5. Reflection coefficient for each designing step

In the first step, we inserted rectangular slots into the lower patch to create a spiral antenna; similarly, we introduced slots into the upper radiating element to design a ring-shaped patch. We can see the appearance of two resonances, one at 4.1 GHz and the other at 5.86 GHz. For both, the reflection coefficient value was greater than -10 dB, but they're nevertheless pretty large. To match the operating frequencies of 2.4 GHz and 5.8 GHz for the low and high resonance frequencies, respectively, we had to sweep the operating frequencies slightly towards the lower frequencies. In the second step, we compressed the spiral shape of the lower patch and positioned it in the center of the radiating element. We inserted two rectangular

slots on the patch's borders, which optimized the reflection coefficient from -11.1 dB to -16 dB in the low frequencies and from -18 dB to -21 dB near the high frequencies, despite not tuning the resonant frequencies to the desired resonant frequencies. In the third step (Figure 4), we introduced additional slots on the two patches to extend the current path and shift the frequencies towards the low frequencies. Figure 5 clearly shows that we have brought the resonance frequencies closer to the suitable frequencies, significantly improving the adaptation and optimizing the reflection coefficient values. In the last step, we only added a resistance on the upper patch, which allows for more optimized results. We moved the resonance at lower frequencies from 2.38 GHz to 2.4 GHz, exhibiting a reflection coefficient of -47 dB. On the other side, the upper resonance (5.75 GHz) showed an S_{11} value of -34 dB. The insertion of parasitic elements not only makes it possible to develop the miniaturization of the antennas, but it is also a means of adapting them.

2.4. Parametric analysis

This section displays the parametric analysis of the proposed antenna. This analysis allows both adjustment and optimization of the results. We adopt the same eyeball phantom model from Figure 2(a) for this parametric study, positioning the antenna once again in the phantom to evaluate the impact of modifications to the antenna design parameters on the reflection coefficient. During the parametric study of the proposed antenna, it is crucial to take into account the positioning of the feed and the resistor's value and placement. We have carefully chosen all these factors to make adjusting the proposed antenna easy.

2.4.1. Impacts of the position of the feed

When using the proposed antenna, Figure 6 shows how changes in feed position impact S_{11} . It is clear that the feed's position is critical to achieving dual-band. Feeding the antenna at P3 generates a resonance with a 400 MHz bandwidth at 6.5 GHz. Even though the antenna exhibits three weak resonant modes at about 2.5 GHz, 4.19 GHz, and 5.7 GHz when stimulated at P4, the matching problem persists. Similar to the previous example, maintaining the feed at P2 leads to a single strong resonance at 6.5 GHz. However, stimulating the antenna at P1 yields a better resonant frequency match. Our study leads us to the conclusion that P4 is the optimal feeding location to obtain dual-band capacity with satisfactory bandwidths.

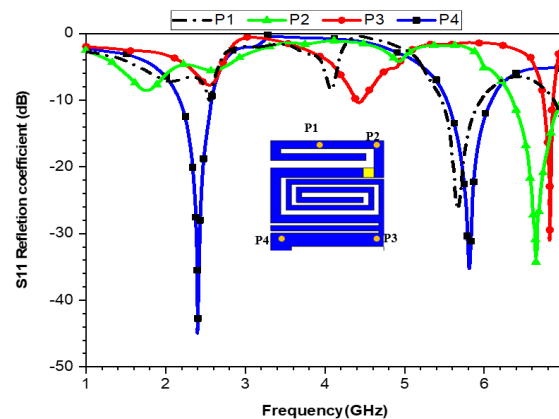


Figure 6. Effects on S_{11} due to variations in feed position

2.4.2. The impact of changing the values and position of introducing resistor

In this study, the value of the resistor element was one of the main parameters used to determine the appropriate bandwidth for the required antenna, which significantly reduced the size. Figure 7 shows how the reflection coefficient varies with the different positions of the supply resistor. The placement of the resistor significantly influences the antenna's matching performance. At position 1, the antenna doesn't match the impedance well at first, so the low resonance frequency moves above the intended frequency and the reflection coefficients for both the low and high resonances are higher than -10 dB. When moved to the second position, the antenna improves slightly in adaptation but does not achieve the desired frequency tuning. The reflection coefficient values measured are -11 dB, -22 dB, and -27 dB at 2.2 GHz, 2.85 GHz, and 6.68 GHz, respectively. In the third position, although there is still a frequency tuning issue, there is an improvement in adaptation compared to the second position. Finally, relocating the resistor from position 3 to position 4, as depicted in Figure 7, achieves the desired frequency band. The antenna exhibits excellent adaptation with reflection coefficients of -44 dB and -34 dB at frequencies of 2.4 GHz and 5.75 GHz, respectively.

Determining the optimal resistance value for 'L. R' was crucial to achieve excellent results once we determined the optimal position for the resistor. Figure 8 shows a comparison of the reflection coefficient

using various resistance values to connect the lower patch to the substrate ground. According to the findings, an increase in resistance value causes the resonant frequency to shift towards a lower frequency range, demonstrating the significant impact of resistance on the operational frequency band. Setting the resistance value L.R. to 3 ohms resulted in reflection coefficients of -16 dB and -27 dB at frequencies 2.46 GHz and 5.85 GHz, respectively. Increasing the L.R. value by 2 ohms (L.R.=5 ohms) caused the resonant frequencies to shift from 2.46 GHz to 2.4 GHz and from 5.85 GHz to 5.75 GHz. This adjustment optimized the reflection coefficient values, as illustrated in Figure 7, where the simulated S_{11} values were -24 dB and -34 dB at the low and high resonance frequencies, respectively. However, setting the value of L.R. to 7 ohm caused the low resonance frequency to shift below the desired frequency, leading to a degradation of impedance matching at lower frequencies when the resistor value was equal to 10 ohm. The results shown in Figure 8 suggest that the optimal choice for achieving dual-band with satisfactory bandwidths is to use a 5-ohm resistor.

By the same procedure, we determined the optimal position of the resistor inserted in the upper patch, followed by the determination of the best value of the resistor. Figure 9 illustrates that the placement of the resistance has a significant influence on the reflection coefficient. Locating the resistor at P1 yields S_{11} values of -42 dB and -13 dB at frequencies of 2.39 GHz and 5.77 GHz, respectively, while placing the resistor at P2 yields S_{11} values of -38 dB and -20 dB at frequencies of 2.2 GHz and 5.77 GHz, respectively. The results demonstrate that the P3 position generates a reflection coefficient of -45 dB and -35 dB at frequencies of 2.4 GHz and 5.77 GHz, respectively. Furthermore, Figure 10 shows that the value of the top resistor (U.R.) significantly impacts impedance matching and fine-tuning capability at the desired frequency. Setting U.R. to 3.5 ohms allows the antenna to display acceptable bandwidths throughout the operating frequency range. However, increasing U.R. to lower the resonant frequency is not a linear process. These findings underscore the crucial role of parametric optimization in achieving impedance matching, tuning, and desired frequency outcomes.

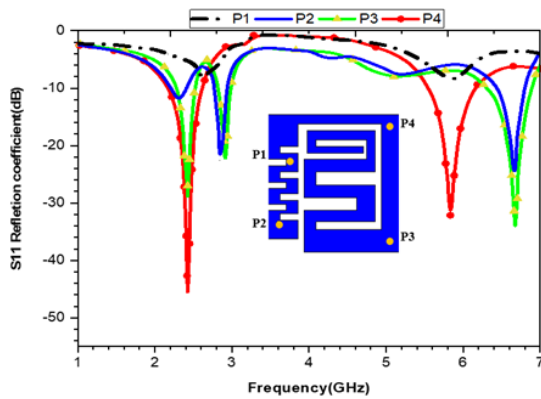


Figure 7. Effect of varying the position of the lower resistor

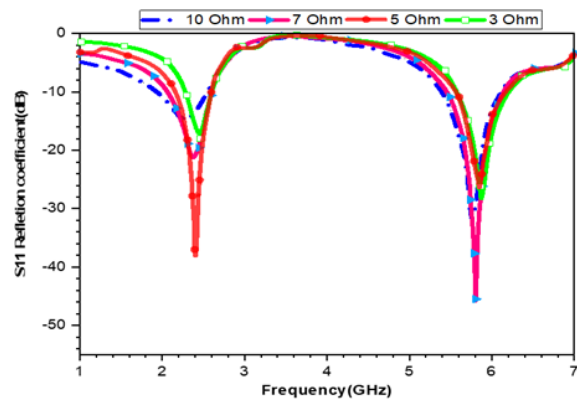


Figure 8. Effect of varying values of the lower resistor

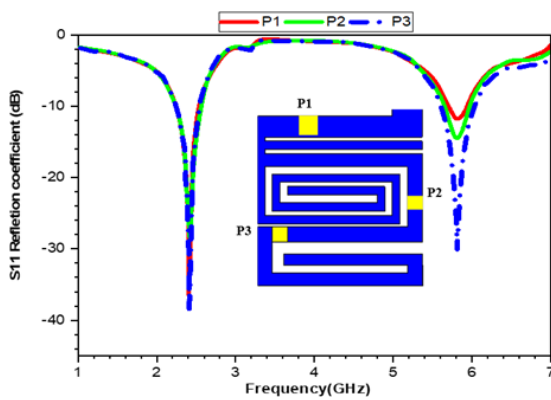


Figure 9. Effect of varying position of upper resistor

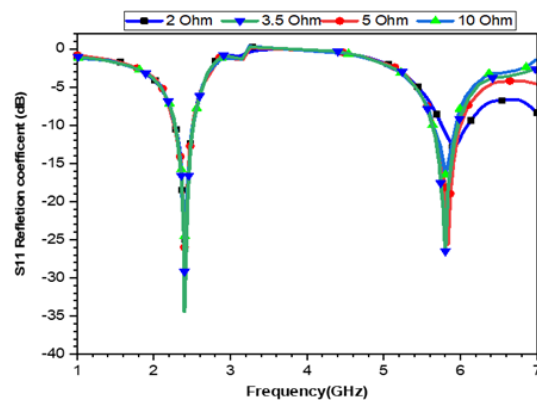


Figure 10. Effect of varying values of upper resistor

2.4.3. Coupling effects due to antenna integration with retinal prosthesis

So far, we have designed and simulated the antenna without integrating it into the implant (retinal prosthesis). However, in a workplace setting, electronics, a power manager, and other components will encapsulate the antenna, as illustrated in Figure 2(b), leading to coupling issues between the system's components and the proposed antenna. Figure 3(a) illustrates the analysis of this coupling by placing the entire system in the adopted phantom model. The results clearly indicate that our antenna is less sensitive to coupling effects. This can be attributed to the implementation of a biocompatibility layer that effectively covers the entire antenna system, including the superstrate positioned above the top patch. After integrating the antenna with the implant, we increased the reflection coefficient for both resonances, resulting in S_{11} values of -24 dB and -22 dB at 2.4 GHz and 5.9 GHz, respectively. We also observed a detuning near the high resonance, shifting it from 5.78 GHz to 5.9 GHz. In order to tune this resonance and optimize the antenna, a small parametric study was performed. The results obtained after optimization were almost the same, or the antenna was no longer encapsulated with the implant, as shown in Figure 11.

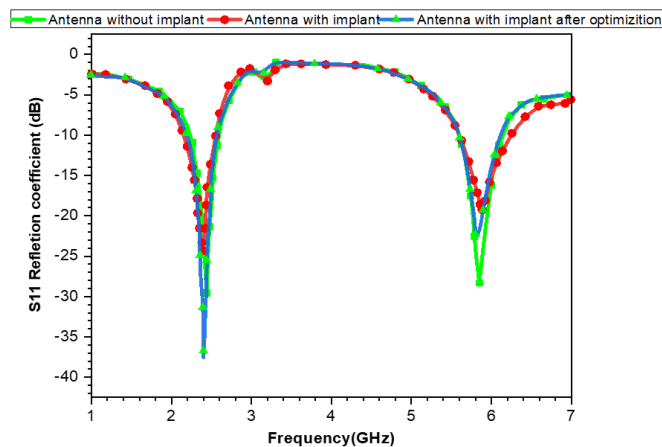


Figure 11. Reflection coefficient S_{11} in the different scenarios

3. RESULTS AND DISCUSSION

In the initial phase of the investigation, the focus centered on the modeling, analysis, and validation of an antenna primarily designed for reception and intended for implantation within the human eye. Subsequently, we introduced a transmitting antenna with dual objectives: to facilitate energy transfer to the implanted component through microwave feeding, and to enable the communication of biological data via telemetry. Energy transmission is a fundamental component of biological systems, with the setup employing the planned wireless power transfer (WPT) transmitter as the source and the implanted antenna as the receiver. The second part aims to create a high-performance rectangular patch antenna that works as a WPT. This is an important part for sending RF energy to deeply embedded implants to power them and for sending biological information.

We add slots to the patch and ground plane to miniaturize and adapt the antenna, following parametric studies to identify the optimal antenna characteristics, as shown in Figure 12. Figures 12(a), 12(b), and 12(c) depict the top view, bottom view, and antenna position of the proposed geometry and external antenna, respectively. The FR4-EPOXY substrate, with a thickness of 1.6 mm, forms the radiating components of the antenna. Overall, the WPT transmitter is $36 \times 36 \times 1.6 \text{ mm}^3$. The simulations position the WPT transmitter at a distance of 2 cm from the ocular lens and 3 cm from the implanted antenna, as shown in Figure 12(c).

Figure 13 displays the system's S_{21} values at 2.4 GHz and 5.8 GHz frequencies, registering magnitudes of -15.09 dB and -17.0 dB, respectively. Figures 13(a) and 13(b) depict the HFSS and CST used in simulated S-parameters for implantable and transmitter antennas, respectively. Additionally, we measure the reflection coefficients at these frequencies to be -32 dB and -27.1 dB, respectively. S_{21} represents the system's transmission coefficient, while S_{11} and S_{22} stand for the WPT transmitters and the implanted antenna's respective reflection coefficients. We use (1) to calculate the power transfer efficiency (PTE) of the WPT system. The system obtains PTE values of 16.01% and 12.86%, respectively, for frequencies of 2.4 GHz and 5.8 GHz.

$$PTE(\%) = |S_{21}|^2(1 - |S_{11}|^2)(1 - |S_{22}|^2) \times 100 \quad (1)$$

These findings show that the implantable receiving antenna can precisely adapt to the needs of the human eye, proving that it is important for medical uses. Moreover, the elevated power transfer efficiency values underscore the effectiveness of the proposed system for energy transfer, emphasizing its potential for advancing biomedical technologies.

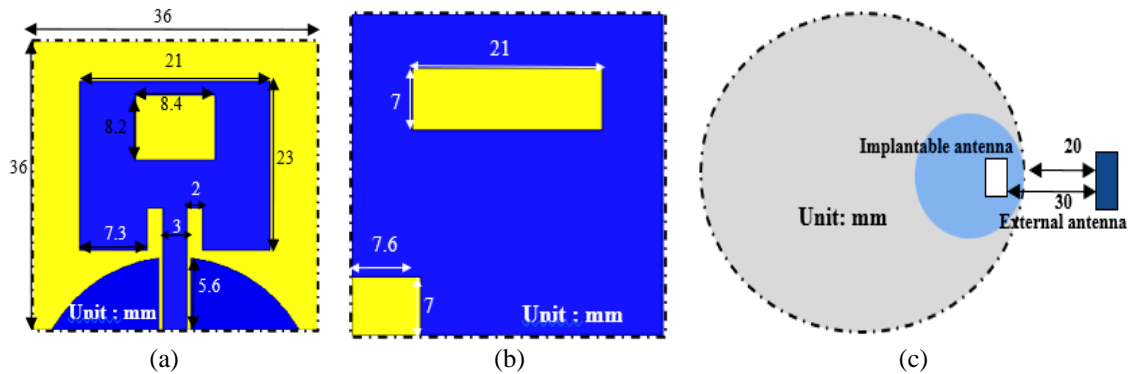


Figure 12. Proposed geometry and position for the external antenna: (a) top view, (b) bottom view, and (c) antenna position

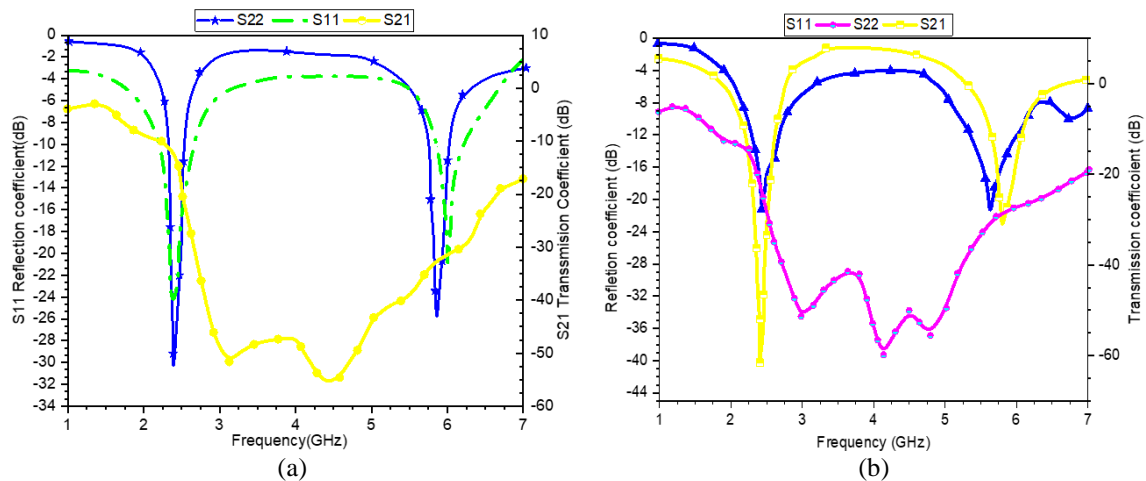


Figure 13. Simulated S-parameters of implantable and transmitter antennas using (a) HFSS and (b) CST

The implantable antenna evidently captures a significant portion of the WPT transmitter's emitted power due to the dispersive nature of the propagation environment. Effective communication within the retinal implant system, whether implanted or not, depends on the antenna's ability to emit strongly and directly towards the intended target, such as the receiving antenna in downlink communication. The results shown in Figure 14 depict the implantable antenna's polar radiation pattern at frequencies of 2.4 GHz and 5.8 GHz. The phantom measured the implantable antenna's peak gains at -27.76 dB, -28.61 dB, and -28.00 dB at 2.4 GHz, and -16.40 dB, -17.38 dB, and -17.00 dB at 5.8 GHz, respectively, with and without the integrated device. Figures 14(a) and 14(b) depict the far-field polar gain patterns of an implantable antenna at 2.4 GHz and 5.8 GHz, respectively. Furthermore, Figure 15 showcases the radiation efficiency values for the two resonances of the implantable antenna, both pre- and post-retuning. Figures 15(a) and 15(b) depict the efficiency of the conformal antenna in different implantation scenarios at 2.4 GHz and 5.8 GHz, respectively. Radiation absorption and significant tissue interaction often substantially diminish antenna efficacy after implantation in eye tissue. The findings underscore the robust performance and adaptability of the implantable antenna, demonstrating its efficacy in the challenging environment of eye tissue implantation.

The variability in efficiency, influenced by implantation depth and tissue type, highlights the intricate challenges faced by implantable antennas, often operating at efficiencies of 1% or less. Notably, optimization efforts have notably enhanced antenna efficiency. We observed radiation efficiency values at 2.4 GHz of -32.42 dBi, -32.95 dBi, and -32.39 dBi, with corresponding values at 5.8 GHz. Integration with the device yielded further improvements, as evidenced by -22.65 dBi, -22.79 dBi, and -22.75 dBi without integration, respectively, as illustrated in Figure 15. Figure 16 depicts the transmitting antenna's far-field polar gain patterns at 2.4 GHz and 5.8 GHz. We can clearly see that the antenna can distribute and concentrate the power in the implantable antenna sufficiently without any problem.

We recommend the adoption of external antennas to address the inherent limitations of antennas and strengthen the link budget, as they offer superior efficiency and performance. Simulations conducted using CST software corroborated the results obtained with HFSS software, validating the accuracy and reliability of our findings. Figure 17 shows the simulated gain and radiation efficiency of implantable. At 2.4 GHz, the implantable antenna had modeled gains of -29 dBi and -35 dBi using HFSS and CST software, respectively. It also had efficiencies of 0.07% and 0.06% near the first resonance. At 5.8 GHz, efficiencies peaked at 0.60% and 0.51%, with modeled gains of -21.2 dBi and -16.40 dBi for CST and HFSS simulations, respectively, as illustrated in Figure 17(a). At 2.4 GHz, the transmitting antenna exhibited modeled gains of 2.18 dBi and 2.21 dBi, with efficiencies of 60% and 63% using HFSS and CST software, respectively. At 5.8 GHz, the modeled gains were 4.21 dBi and 4.2 dBi, with efficiencies of 65% and 66%, as illustrated in Figure 17(b). The results show how optimization is a key factor in improving the performance and usability of implantable antennas. They show how these antennas could change biomedical applications by providing better performance and more operational options.

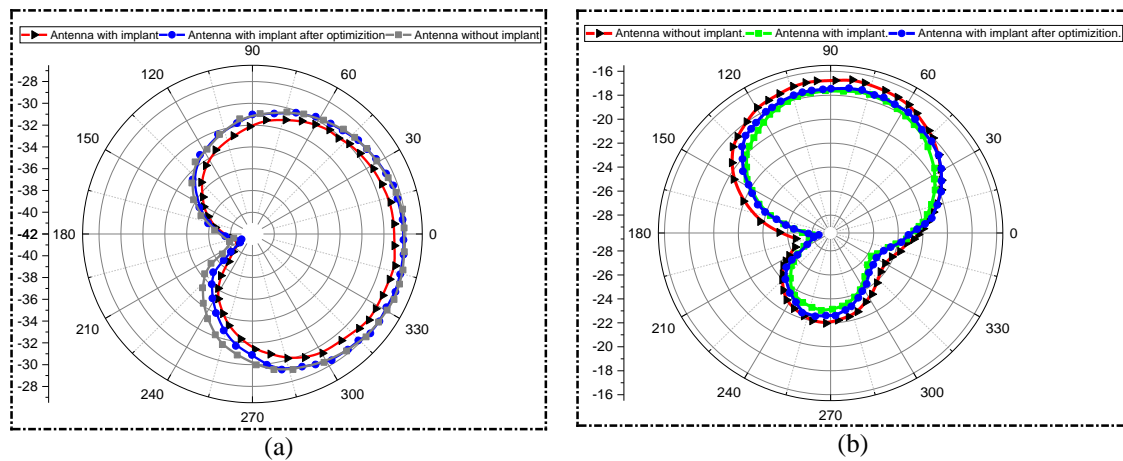


Figure 14. Far-field polar gain patterns of implantable antenna (a) at 2.4 GHz and (b) at 5.8 GHz

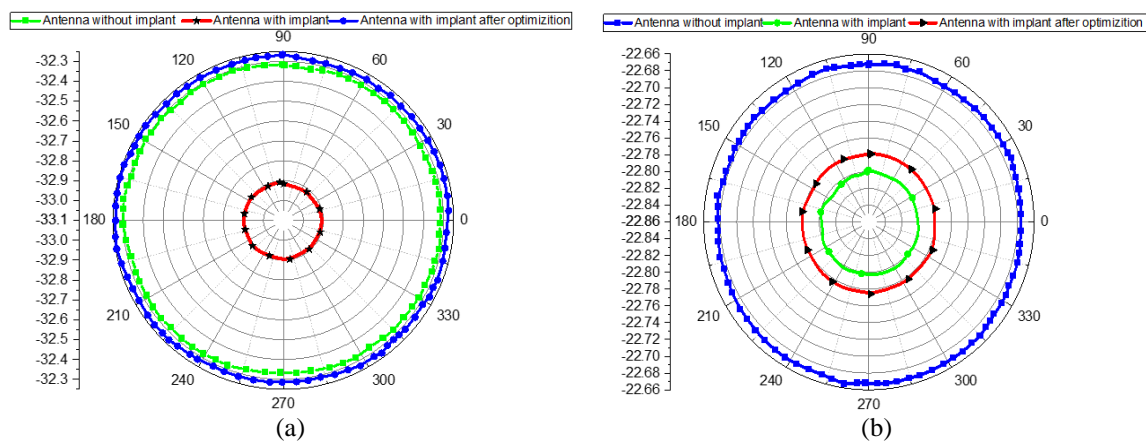


Figure 15. Efficiency of the conformal antenna in different implantation scenarios (a) at 2.4 GHz and (b) at 5.8 GHz

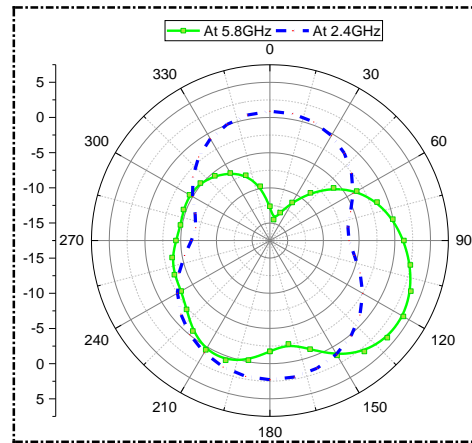


Figure 16. Far-field polar gain patterns of transmitter antenna at 2.4 GHz and 5.8 GHz

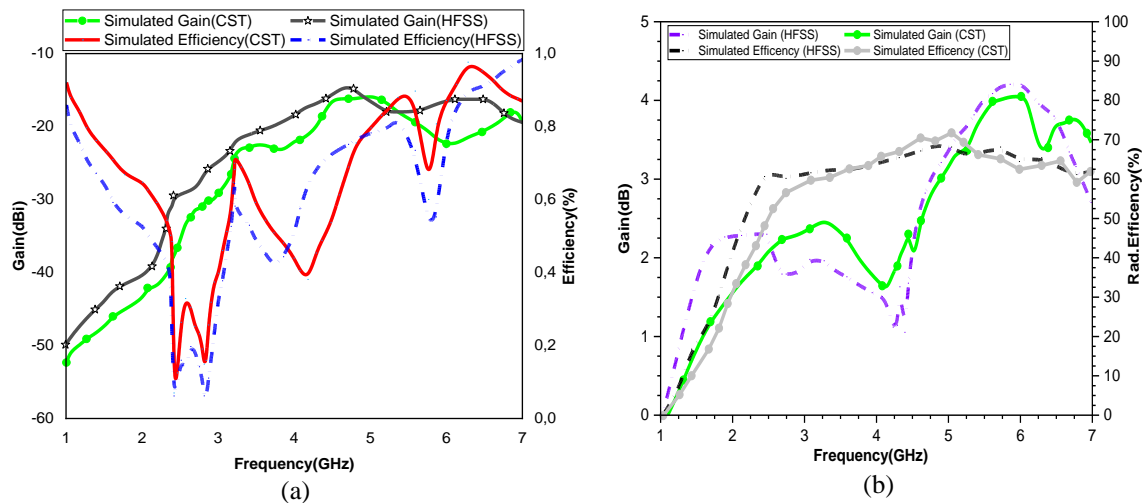


Figure 17. Simulated gain and radiation efficiency of implantable: (a) transmitter and (b) antennas using HFSS and CST

Adequate analysis must follow the implantation of medical devices by surgery, especially those with radiative components, to reduce the side effects brought on by this radiation. The safety of people, especially patients, is of utmost importance, and SAR plays a pivotal role in ensuring this. To minimize any possible risks associated with radiation exposure near the human body, the International Committee on Non-ionizing Radiation Protection (ICNIRP) and the Institute of Electrical and Electronics Engineers (IEEE) have imposed SAR limits. It is essential to strictly adhere to the specified limitations, which dictate that the SAR must not exceed 1.6 W/kg on average over 1 g of tissue and 2 W/kg on average over 10 g of tissue [13], [14]. As an adult's entire eyeball typically weighs between 11 and 12 g [25], SAR measurement beyond 10 g is not relevant in this context. Instead, we measure SAR for just 1 g of tissue at various frequencies using HFSS in an eye model. To evaluate the safety of our system, we analyzed the SAR at 1 g for both frequencies (2.4 and 5.8 GHz). The implanted antenna only served as a receiver for WPT at 5.8 GHz, broadcasting at 2.4 GHz on the implant side. Therefore, we conducted a 2.4 GHz SAR analysis on the implanted antenna in the phantom model at 1 g, as shown in tabure 19. At this weight, the highest SAR levels for 2.4 GHz and 5.8 GHz frequencies were 5.12 W/kg and 1.7 W/kg, respectively. However, the maximum SAR value for the implanted antenna in the phantom model was 262.9 W/kg. It should be emphasized that there is a correlation between input power and SAR, according to sources [26]-[29].

$$SAR = \frac{\sigma|E|^2}{\rho} \quad (2)$$

In (3) establishes a relationship between electric power intensity and signal strength, given by the expression, where represents electrical conductivity σ (S/m) and denotes mass density ρ (kg/m³) [29]. Additionally, E corresponds to the electrical field intensity (V/m). The above equation indicates an inverse correlation between the intensity of the electrical energy and the intensity of the signal.

$$P = \frac{[E(V/m)]^2}{377} \tag{3}$$

Figure 18 shows that the implanted antenna meets safety requirements with a power threshold of 5.9 mW, equivalent to a SAR of 1.5 W/kg. This threshold denotes the highest input power allowed under the 1 g standard, which can be harmful to the human eye if exceeded. Figures 18(a) and 18(b) show the simulation results for the implantable antenna's 1-g SAR distribution at 2.4 GHz with input power of 1 and 0.94 W. The TX antenna consistently shows maximum SAR values below the 1.6 W/kg threshold, which is rather excellent. The TX antenna operates at input energies of 0.94 W and 0.30 W, respectively. Figures 19 and 20 show that the SAR values remain below 1.6 W/kg for frequencies of 2.4 GHz and 5.8 GHz. Note that these numbers significantly exceed the specified 25 W transmit power in [12]. Figures 19(a) and 19(b), respectively, display the simulation of the distribution of 1-g SAR for a Tx antenna at 2.4 GHz with input power of 1 and 0.94 W. Figures 20(a) and 20(b) show the simulation of the 1-g SAR distribution for a Tx antenna at 5.8 GHz with 1 W of input power and 0.94 W of input power, respectively.

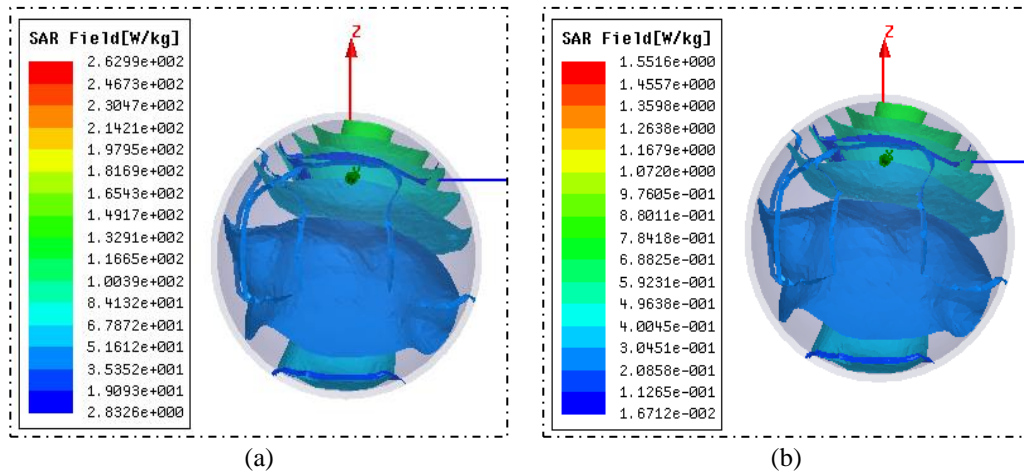


Figure 18. Simulation results of implantable antenna' 1-g SAR distribution at 2.4 GHz with input power of (a) 1 W and (b) 0.94 W

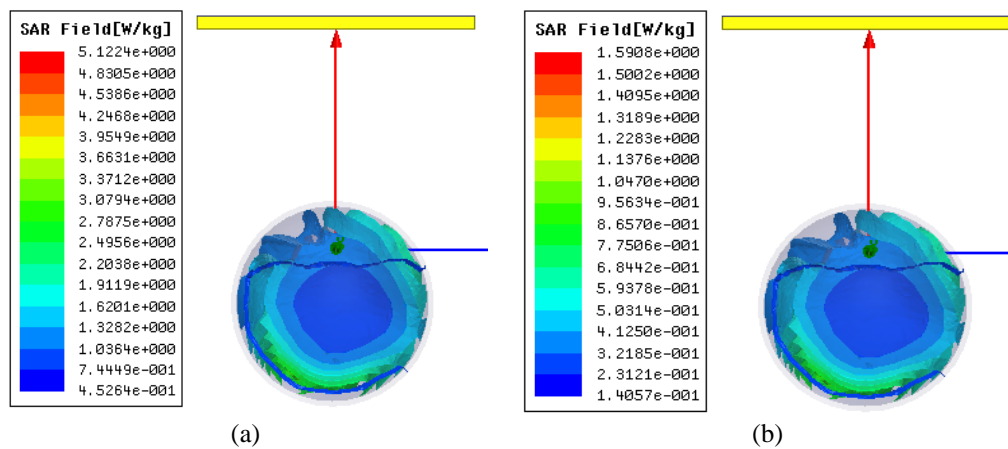


Figure 19. Simulating the distribution of 1-g SAR for Tx antenna at 2.4 GHz with input power of (a) 1 W and (b) 0.94 W

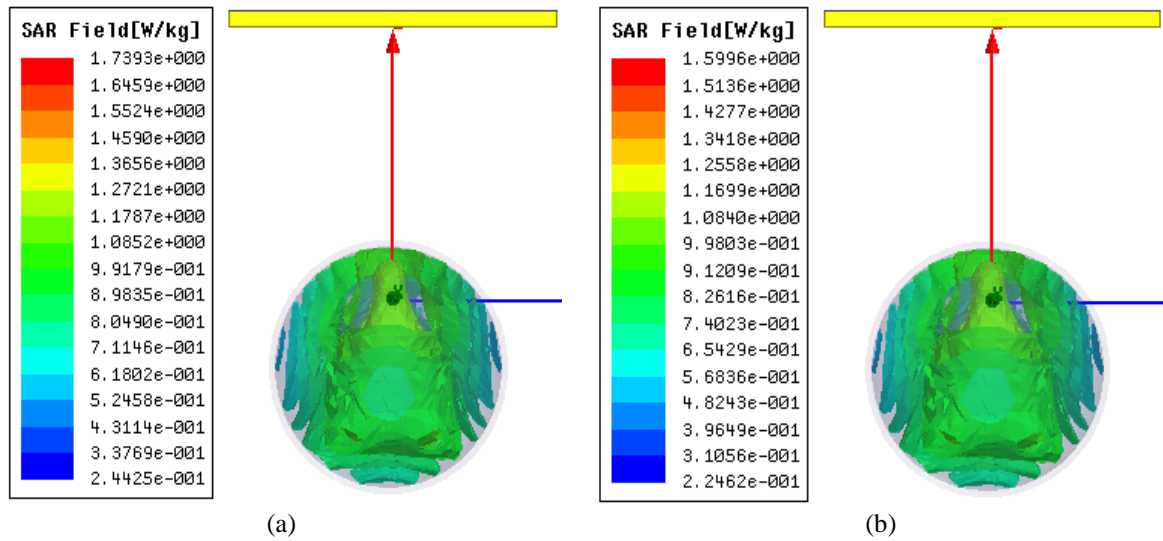


Figure 20. Simulating the distribution of 1-g SAR for Tx antenna at 5.8 GHz with input power of (a) 1 W and (b) 0.30 W

Implantable transducers allow for remote physiological assessments via wireless biomedical communications. The retinal prosthesis has more stimulators than previous functional electrical stimulation (FES) implants. However, to get flicker-free vision at 60 frames per second, it takes a lot of data (614 Kbps) to identify each channel using a 10-bit address in the 1024-channel retinal stimulator [30]. The connection margin is a very important part of making sure that the internal and external parts of the implant can talk to each other without any problems. This is because it can lose signal through reflection, absorption, route attenuation, and polarization change. We employ the Friis equation to determine the link margin, and recommend a link margin of at least 20 dB for coherent communication. Use (4) to compute the necessary antenna power (R_p).

$$R_p = B_r + \frac{E_b}{N_0} + KT \quad (4)$$

The symbols used to represent phase modulation, Boltzmann's constant, temperature, and bit rate are $\frac{E_b}{N_0}$, KT , and B_r , respectively. Additionally, the value of A_p can be determined through (5).

$$A_p(dB) = P_{TX} + G_{TX} + G_{RX} - L_f - P_L \quad (5)$$

Where P_{TX} , G_{TX} , and G_{RX} stand for, respectively, transmitter power maintained at 4 dBm, transmitter antenna gain, and implantable receiver antenna gain. Free space and polarization mismatch losses are denoted by the letters L_f and P_L , respectively. L_f typically relies on the separation (d) of the antennas used for transmission and reception. Formula (6) can be used to calculate this loss.

$$L_f(dB) = 10\delta \log\left(\frac{d}{d_0}\right) + 10 \log\left(\frac{4\pi d_0}{\lambda_0}\right)^2 + S_{(dB)} \quad (6)$$

The formula for link margin involves several variables, including d for distance between antennas, δ for path loss exponent, λ_0 for wavelength in free space, and d_0 for reference distance calculated as $d_0 = \frac{2L^2}{\lambda_0}$, L is the maximum dimension of the antenna in the direction of radiation. Additionally, S represents random dispersion about the mean. The value of δ depends on the propagation environment, for indoor propagation, $\delta=2$, while for open space propagation $\delta=1$ [31]. Table 3 illustrates the parameters employed for calculating the link budget analysis in this study. These parameters are crucial in determining the overall performance and feasibility of the communication system being analyzed.

Figure 21 depicts the link margin as a correlation between the separation distances of the transmitting and receiving antennas. We establish the B_r values as 500 Mb/s, 614 Kb/s, and 4 Gbit/s to

facilitate the transmission of high-quality video from the external antenna to the retinal implant. Establishing a dependable communication link between the implantable and external antennas is crucial, and to attain this objective, it is vital that the antenna power (A_p) surpasses the minimum required power (R_p). Figure 22 plots the received signal strength for both frequencies against distance, showcasing the proposed antenna's efficient communication with the transmitting antenna.

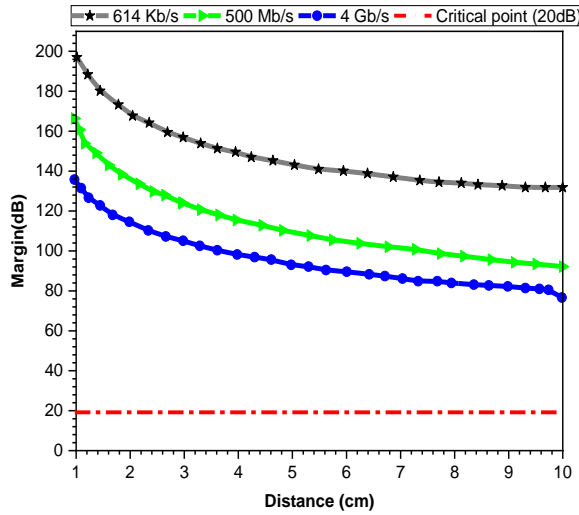


Figure 21. Link margin as a function of distance for different data rates at 2.4 GHz

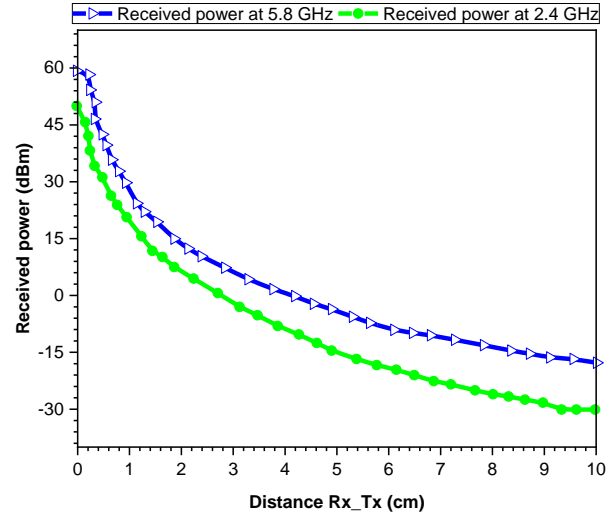


Figure 22. Received signal strength against distance

Table 3. The key parameters taken into consideration for conducting a link budget analysis

Parameters	Variables	Values
Resonance frequency	f_0 (GHz)	2.4-5.8
Noise power density	N_0 (dB/Hz)	-203.93
Transmitter power	P_{TX} (dB_m)	-4
Polarization mismatch loss	P_L (dB)	1
Temperature	T_0 (Kelvin)	273
Path loss	L_f (dB)	Distance dependent
Transmitter antenna gain	G_{TX} (dBi)	$G_{TX}(2.4 \text{ GHz}) = 2.48 \text{ dBi}$ $G_{TX}(5.8 \text{ GHz}) = 4.08 \text{ dBi}$
Receiver antenna gain	G_{RX} (dBi)	$G_{RX}(2.4 \text{ GHz}) = -17 \text{ dBi}$ $G_{RX}(5.8 \text{ GHz}) = -28 \text{ dBi}$
Boltzmann constant	K	1.38×10^{-23}
Available power	A_p (dB)	Distance dependent
Bit rate	B_r	Figure.21
Required power	R_p (dB)	$R_p(614\text{Kb/s}) = -155.89$ $R_p(500\text{Mb/s}) = -111.62$ $R_p(4\text{Gb/s}) = -97.64$
Margin	$A_p - R_p$ (dB)	Fig.21
Path loss exponent	δ	1.5
Shadowing effect	S (dB)	0

Table 4 presents an evaluation of the performance of the proposed antenna in comparison to recent research. In this comparative assessment of antenna performance, our primary focus has been on fulfilling implant specifications. In particular, we have emphasized antenna size, as implantable devices must adhere to stringent size constraints. Our antenna not only meets this critical requirement, but it can also be considered one of the smallest antennas in our knowledge base. Regarding the communication channel, our antenna operates across two frequency bands, each dedicated to a specific type of signaling. This adaptability enhances the versatility of our implantable system. Biocompatibility is another vital aspect of implantable antennas. We encapsulate our antenna in a biocompatible material to ensure its compatibility with the human body. In contrast, many other antennas lack this feature, which is critical for the patient's long-term health. Furthermore, our antenna adheres to SAR safety standards. Despite these demanding constraints, our antenna

exhibits robust performance, which constitutes the primary objective. Our aim is to provide a high-performance antenna that not only meets the security requirements for patient protection but also delivers powerful results.

Table 4. An evaluation of the performance of the proposed antenna in comparison to that of recent research

Ref	Dimensions (mm ³)	Operating Frequency (GHz)	Realized gain (dB)	Operating Bandwidth (%)	SAR (W/kg)	Phantom size (mm ³)	link budget (bit rate)
[9]	7×7×0.2	0.915-2.45	-27.65/-22.99	11.74-23.33	(730.07-591.40) _{ig}	150×150×150	Yes
[10]	19×15×0.2	0.402-0.915-1.200	-30.8-19.7-18.7	38.6-19.6-8.1	(289.0-263.5 - 214.9) _{ig}	10 ² ×10 ² ×20	Yes
[11]	234.95	0.406	-36.64	3.43	497.74- _{ig} Input 1 W	8181.23	-
[12]	7.2×7×0.2	0.902-2.4	-25.65/-28.44	19.83-9.15	(471-313) _{ig} Input 1 W	10 ² ×10 ² ×10 ²	Yes
[18]	7×6.9×0.63	1.45-2.45	-	36	(0.907-1.11) _{ig} Input (88.2-72) mW	Head model using CST	-
[26]	7×7×0.254	0.915	-28	21.85	8.1- _{ig} -Input 0.5W (In body)	12×40×40	-
[32]	9.2×9.2×0.5	2.4-4.8-5.8	-15.8/-15.2 /-16.6 /-15.8	63.87-6.25-1.56-3.44	(350.8-97.9-205-156) _{ig} Input 1W	10 ² ×10 ² ×42	-
[33]	3×3×0.64	2.45-5.8-8	-18.4, -7.6, -4.7	163.6	(792,690,606)- _{ig} Input 1 W	350 ×350×350	-
This work	2.2×2.15×0.78	2.45-5.8	-27.76/-16.40	16.02-9.55	(1.55-1.58) _{ig} Input (5.9-9) mW	8181.23 (eyeball)	Up to 4Gb/s

4. CONCLUSION

This paper has proposed a WPT system with two antennas for retinal implants. The first antenna was implantable (a receiver) and had a compact size of 2.2×2.15×0.78 mm³. The second WPT patch antenna has a volume of 36×36×1.6 mm³ and was located at a distance of 3 cm from the implanted antenna. This second antenna serves two purposes: telemetry transmission and a wireless power supply for recharging the retinal implant. We integrate the proposed antennas with microelectronic components, sensors, batteries, and wire connections to achieve more realistic results, and they resonate at 2.4 GHz and 5.8 GHz in the ISM band. To ensure system safety, we examine the SAR on a human model eye in a heterogeneous environment, taking into account four types of biological tissues. We also evaluate the link budget for far-field communication between the retinal implant and external antenna. The proposed antenna system's simulation results obtained using HFSS and CST demonstrate excellent agreement.

REFERENCES

- [1] R. Chandra and A. J. Johansson, "A link loss model for the on-body propagation channel for binaural hearing aids," *IEEE Transactions on Antennas and Propagation*, vol. 61, no. 12, pp. 6180–6190, Dec. 2013, doi: 10.1109/TAP.2013.2283270.
- [2] M. M. Soliman *et al.*, "Review on medical implantable antenna technology and imminent research challenges," *Sensors*, vol. 21, no. 9, 2021, doi: 10.3390/s21093163.
- [3] S. A. A. Shah and H. Yoo, "Scalp-implantable antenna systems for intracranial pressure monitoring," *IEEE Transactions on Antennas and Propagation*, vol. 66, no. 4, pp. 2170–2173, Apr. 2018, doi: 10.1109/TAP.2018.2801346.
- [4] I. Gani and H. Yoo, "Multi-band antenna system for skin implant," *IEEE Microwave and Wireless Components Letters*, vol. 26, no. 4, pp. 294–296, Apr. 2016, doi: 10.1109/LMWC.2016.2538470.
- [5] C. Liu, Y. X. Guo, and S. Xiao, "Compact dual-band antenna for implantable devices," *IEEE Antennas and Wireless Propagation Letters*, vol. 11, pp. 1508–1511, 2012, doi: 10.1109/LAWP.2012.2233705.
- [6] A. Rahman *et al.*, "Electromagnetic performances analysis of an ultra-wideband and flexible material antenna in microwave breast imaging: to implement a wearable medical bra," *Scientific reports*, vol. 6, p. 38906, 2016, doi.org/10.1038/srep38906.
- [7] A. Kiourti and K. S. Nikita, "Antennas and RF Communication," *Handbook of Biomedical Telemetry*, pp. 209–251, 2014, doi: 10.1002/9781118893715.ch8.
- [8] A. Kiourti, K. A. Psathas, and K. S. Nikita, "Implantable and ingestible medical devices with wireless telemetry functionalities: a review of current status and challenges," *Bioelectromagnetics*, vol. 35, no. 1, pp. 1–15, 2014, doi: 10.1002/bem.21813.
- [9] F. Faisal, M. Zada, A. Ejaz, Y. Amin, S. Ullah, and H. Yoo, "A miniaturized dual-band implantable antenna system for medical applications," *IEEE Transactions on Antennas and Propagation*, vol. 68, no. 2, pp. 1161–1165, 2020, doi: 10.1109/TAP.2019.2938591.
- [10] Y. Alamgir *et al.*, "Compacted conformal implantable antenna with multitasking capabilities for ingestible capsule endoscope," *IEEE Access*, vol. 8, pp. 157617–157627, 2020, doi: 10.1109/ACCESS.2020.3019663.
- [11] O. Liapatis and K. S. Nikita, "Development of a biocompatible patch antenna for retinal prosthesis: comparison of biocompatible coatings," in *Proceedings - IEEE 20th International Conference on Bioinformatics and Bioengineering, BIBE 2020*, Oct. 2020, pp. 819–825, doi: 10.1109/BIBE50027.2020.00139.

- [12] F. Faisal and H. Yoo, "A miniaturized novel-shape dual-band antenna for implantable applications," *IEEE Transactions on Antennas and Propagation*, vol. 67, no. 2, pp. 774–783, 2019, doi: 10.1109/TAP.2018.2880046.
- [13] Institute of Electrical and Electronics Engineers, "IEEE standard for safety levels with respect to human exposure to electric, magnetic, and electromagnetic fields, 0 Hz to 300 GHz," *IEEE C95.1-2019*, 2020.
- [14] Institute of Electrical and Electronics Engineers, "IEEE standard for safety levels with respect to human exposure to radio frequency electromagnetic fields, 3 kHz to 300 GHz," *IEEE Std C95.1*, pp. 1–83, 1999.
- [15] P. Saha, D. Mitra, and S. K. Parui, "A circularly polarized implantable monopole antenna for biomedical applications," *Progress In Electromagnetics Research C*, vol. 85, pp. 167–175, 2018, doi: 10.2528/pierc18051807.
- [16] Z. Bao, Y. X. Guo, and R. Mittra, "Single-layer dual-/tri-band inverted-f antennas for conformal capsule type of applications," *IEEE Transactions on Antennas and Propagation*, vol. 65, no. 12, pp. 7257–7265, 2017, doi: 10.1109/TAP.2017.2758161.
- [17] M. Zada and H. Yoo, "A miniaturized triple-band implantable antenna system for bio-telemetry applications," *IEEE Transactions on Antennas and Propagation*, vol. 66, no. 12, pp. 7378–7382, 2018, doi: 10.1109/TAP.2018.2874681.
- [18] S. Bahrami, G. Moloudian, S. R. Miri-Rostami, and T. Bjorninen, "Compact microstrip antennas with enhanced bandwidth for the implanted and external subsystems of a wireless retinal prosthesis," *IEEE Transactions on Antennas and Propagation*, vol. 69, no. 5, pp. 2969–2974, 2021, doi: 10.1109/TAP.2020.3025245.
- [19] W. Mokwa, M. Goertz, C. Koch, I. Krisch, H. K. Trieu, and P. Walter, "Intraocular epiretinal prosthesis to restore vision in blind humans," *Proceedings of the 30th Annual International Conference of the IEEE Engineering in Medicine and Biology Society, EMBS'08 - "Personalized Healthcare through Technology"*, pp. 5790–5793, 2008, doi: 10.1109/iembs.2008.4650530.
- [20] P. A. Hasgall *et al.*, "Data base for thermal and electromagnetic parameters of biological tissues, Version 4.1," 2022, doi: 10.13099/VIP21000-04-1.
- [21] E. Bloch, Y. Luo, and L. da Cruz, "Advances in retinal prosthesis systems," *Therapeutic Advances in Ophthalmology*, vol. 11, p. 251584141881750, Jan. 2019, doi: 10.1177/2515841418817501.
- [22] A. Bellapianta, A. Cetkovic, M. Bolz, and A. Salti, "Retinal organoids and retinal prostheses: an overview," *International Journal of Molecular Sciences*, vol. 23, no. 6, p. 2922, Mar. 2022, doi: 10.3390/ijms23062922.
- [23] S. Kim and H. Shin, "An ultra-wideband conformal meandered loop antenna for wireless capsule endoscopy," *Journal of Electromagnetic Engineering and Science*, vol. 19, no. 2, pp. 101–106, 2019, doi: 10.26866/JEES.2019.19.2.101.
- [24] A. Kiourti and K. S. Nikita, "A review of implantable patch antennas for biomedical telemetry: challenges and solutions," *IEEE Antennas and Propagation Magazine*, vol. 54, no. 3, pp. 210–228, 2012, doi: 10.1109/MAP.2012.6293992.
- [25] L. Li, N. K. Nikolova, and N. T. Sangary, "Evaluation of the specific absorption rate and the temperature rise in the human eyes with account for resonance," *IEEE Transactions on Microwave Theory and Techniques*, vol. 57, no. 12, pp. 3450–3460, 2009, doi: 10.1109/TMTT.2009.2033858.
- [26] S. Ahmad, B. Manzoor, S. Naseer, N. Santos-Valdivia, A. Ghaffar, and M. I. Abbasi, "X-shaped slotted patch biomedical implantable antenna for wireless communication networks," *Wireless Communications and Mobile Computing*, vol. 2022, 2022, doi: 10.1155/2022/7594587.
- [27] L. J. Xu, Y. Bo, W. J. Lu, L. Zhu, and C. Guo, "Circularly polarized annular ring antenna with wide axial-ratio bandwidth for biomedical applications," *IEEE Access*, vol. 7, pp. 59999–60009, 2019, doi: 10.1109/ACCESS.2019.2915236.
- [28] R. Li, B. Li, G. Du, X. Sun, and H. Sun, "A compact broadband antenna with dual-resonance for implantable devices," *Micromachines*, vol. 10, no. 1, 2019, doi: 10.3390/mi10010059.
- [29] K. K. Naik, S. C. S. Teja, B. V. S. Sailaja, and P. A. Vijaya Sri, "Design of flexible parasitic element patch antenna for biomedical application," *Progress In Electromagnetics Research M*, vol. 94, pp. 143–153, 2020, doi: 10.2528/pierm20030406.
- [30] Y. K. Lo, K. Chen, P. Gad, and W. Liu, "A fully-integrated high-compliance voltage SoC for epi-retinal and neural prostheses," *IEEE Transactions on Biomedical Circuits and Systems*, vol. 7, no. 6, pp. 761–772, 2013, doi: 10.1109/TBCAS.2013.2297695.
- [31] A. Alomainy and Y. Hao, "Modeling and characterization of biotelemetric radio channel from ingested implants considering organ contents," *IEEE Transactions on Antennas and Propagation*, vol. 57, no. 4 PART. 1, pp. 999–1005, 2009, doi: 10.1109/TAP.2009.2014531.
- [32] S. S. Mosavinejad, P. Rezaei, A. A. Khazaei, and J. Shirazi, "A triple-band spiral-shaped antenna for high data rate fully passive implantable devices," *AEU - International Journal of Electronics and Communications*, vol. 159, 2023, doi: 10.1016/j.aeue.2022.154474.
- [33] V. Kaim, B. K. Kanaujia, S. Kumar, H. C. Choi, K. W. Kim, and K. Rambabu, "Electrically small circularly polarized UWB intraocular antenna system for retinal prosthesis," *IEEE Transactions on Biomedical Engineering*, vol. 69, no. 11, pp. 3504–3515, 2022, doi: 10.1109/TBME.2022.3171842.

BIOGRAPHIES OF AUTHORS



Abdelmouttalib Bousrout     received a specialized Master's degree in Telecommunication Systems at Ibn Tofail University in 2021 after earning a Bachelor of Physics degree with an electronics concentration from Cadi Ayyad University in 2018. He is currently pursuing her doctorate in signal processing and telecommunication at Ibn Tofail University in Kenitra, Morocco. Two of his main areas of interest are miniaturization and the development of high-performing antennas for biomedical applications. He can be contacted at email: abdelmouttalib1995@gmail.com.



Asma Khabba    obtained a Master of Science in Control, Industrial Computing, Signals, and Systems from Cadi Ayyad University in 2017 after completing her Bachelor of Science in Physics there in 2015. She is currently a Ph.D. candidate at Cadi Ayyad University in Marrakech, Morocco, studying signal processing and telecommunications. Phased arrays, MIMO antennas, millimeter wave and microwave antennas, and 5G antennas are all areas of interest for her study. She can be contacted at email: asma.khabba@edu.uca.ac.ma.



Saida Ibnyaich    presently serves as professor at Morocco's Cadi Ayyad University in Marrakech. She graduated from Cadi Ayyad University in 2002 with a bachelor's degree in technical sciences, in 2005 with a master's degree in Electrical Engineering with a focus on power electronics and industrial control, and in 2013 with a doctorate in computing and telecommunication. Her areas of interest in research include millimeter waves, PIFA antennas, patch antennas, microwaves, and telecommunications. She can be contacted at email: s.ibnyaich@uca.ac.ma.



Tomader Mazri    a permanent member of the Electrical and Telecommunications Engineering Laboratory and a professor at the National School of Applied Sciences of Kenitra. Ibn Tofail University awarded an HDR degree in networks and telecommunication; Sidi Mohamed BenAbdellah University and INPT of Rabat awarded a Ph.D. degree in microelectronics and telecommunication; a master's degree in microelectronics and telecommunication systems; and Cadi Ayyad University awarded a bachelor's degree in telecommunication. She can be contacted at email: tomader.mazri@uit.ac.ma.



Mohamed Habibi    received his State Doctorate Thesis in Electronics from Mohammed University V of Mohammadia Engineering School of Rabat, Morocco, in 1993, and his 3rd Cycle University Thesis in Electronics from the University of Sciences and Technologies of Lille Flandres Artois, France, in 1985. He is currently employed by Ibn Tofail University in Kenitra, Morocco, as a member of the laboratory of electronic systems, information processing, mechanics, and energy. His work focuses on applications using microwaves. He can be contacted at email: habibi.mohamed@uit.ac.ma.



Tole Sutikno    is a lecturer and the head of the Master Program of Electrical Engineering at the Faculty of Industrial Technology at Universitas Ahmad Dahlan (UAD) in Yogyakarta, Indonesia. He received his Bachelor of Engineering from Universitas Diponegoro in 1999, Master of Engineering from Universitas Gadjah Mada in 2004, and Doctor of Philosophy in Electrical Engineering from Universiti Teknologi Malaysia in 2016. All three degrees are in electrical engineering. He has been a Professor at UAD in Yogyakarta, Indonesia, since July 2023, following his tenure as an Associate Professor in June 2008. He is the Editor-in-Chief of TELKOMNIKA and Head of the Embedded Systems and Power Electronics Research Group (ESPERG). He is one of the top 2% of researchers worldwide, according to Stanford University and Elsevier BV's list of the most influential scientists from 2021 to the present. His research interests cover digital design, industrial applications, industrial electronics, industrial informatics, power electronics, motor drives, renewable energy, FPGA applications, embedded systems, artificial intelligence, intelligent control, digital libraries, and information technology. He can be contacted at email: tole@te.uad.ac.id.